Earth and Planetary Science Letters 608 (2023) 118036

Contents lists available at ScienceDirect

Earth and Planetary Science Letters

journal homepage: www.elsevier.com/locate/epsl

The influence of erosion and vegetation on soil production and chemical weathering rates in the Southern Alps, New Zealand

Isaac J. Larsen [a], Andre Eger [b], Peter C. Almond [c], Evan A. Thaler [a,d], J. Michael Rhodes [a], Günther Prasicek [e,f,g]

[a] University of Massachusetts, Department of Geosciences, Amherst, MA 01003-9297, USA
[b] Landcare Research, Department Soil and Landscapes, 54 Gerald St, Lincoln 7608, New Zealand
[c] Lincoln University, Department of Soil and Physical Sciences, PO Box 85084, Lincoln 7647, New Zealand
[d] Earth and Environmental Sciences Division, Los Alamos National Laboratory, Los Alamos, NM, USA [1]
[e] University of Lausanne, Interdisciplinary Center for Mountain Research, Switzerland
[f] University of Salzburg, Department of Geography and Geology, Austria
[g] Vexcel Imaging, Gratz, Austria [1]

ARTICLE INFO

Article history:
Received 6 September 2022
Received in revised form 28 January 2023
Accepted 28 January 2023
Available online 7 March 2023
Editor: A. Jacobson

Keywords:
soil production
chemical weathering
erosion
vegetation
^{10}Be
New Zealand

ABSTRACT

Chemical weathering influences many aspects of the Earth system, including biogeochemical cycling, climate, and ecosystem function. Physical erosion influences chemical weathering rates by setting the supply of fresh minerals to the critical zone. Vegetation also influences chemical weathering rates, both by physical processes that expose mineral surfaces and via production of acids that contribute to mineral dissolution. However, the role of vegetation in setting surface process rates in different landscapes is unclear. Here we use ^{10}Be and geochemical mass balance to quantify soil production, physical erosion, and chemical weathering rates in a landscape where a migrating drainage divide separates catchments with an order-of magnitude contrast in erosion rates and where vegetation spans temperate rainforest, tussock grassland, and unvegetated alpine ecosystems in the western Southern Alps of New Zealand. Soil production, physical erosion, and chemical weathering rates are significantly higher on the rapidly eroding versus the slowly eroding side of the drainage divide. However, chemical weathering intensity does not vary significantly across the divide or as a function of vegetation type. Soil production rates are correlated with ridgetop curvature, and ridgetops are more convex on the rapidly eroding side of the divide, where soil mineral residence times are lowest. Hence our findings suggest fluvially-driven erosion rates control soil production and soil chemical weathering rates by influencing the relationship between hillslope topography and mineral residence times. In the western Southern Alps, soil production and chemical weathering rates are more strongly mediated by physical rock breakdown driven by landscape response to tectonics, than by vegetation.

1. Introduction

Plate tectonics and plant evolution both influenced chemical weathering rates during the Phanerozoic (Berner, 1990). Plate convergence fractures rock (Molnar et al., 2007) and high rates of physical erosion (e.g., Hovius et al., 1997; Larsen and Montgomery, 2012) in tectonically active landscapes drives chemical weathering of freshly exposed minerals (Millot et al., 2002; Jacobson and Blum, 2003; Riebe et al., 2004a; West, 2012; Larsen et al., 2014; Maher and Chamberlain, 2014). Terrestrial vegetation increases subsurface CO_2 concentrations and releases organic acids, both of which enhance rates of chemical weathering (e.g., Cochran and Berner, 1996; Drever, 1994). Strain generated by plant roots can also fracture rock and generate porosity, which allows water to access the subsurface and increases chemical weathering (Hayes et al., 2019). Hence changes in physical erosion rates caused by the uplift of mountain ranges (Raymo and Ruddiman, 1992) and the evolution of terrestrial vegetation (Berner, 1990) are both thought to influence global-scale chemical weathering rates and climate.

At the hillslope scale, mineral residence time in the weathering zone is set by the physical erosion rate and mobile soil thickness (Almond et al., 2007; Mudd and Yoo, 2010), though saprolite

E-mail address: ilarsen@umass.edu (I.J. Larsen).
[1] Present address.

https://doi.org/10.1016/j.epsl.2023.118036
0012-821X/

weathering can be important in some settings (e.g., Dixon et al., 2009; Eger et al., 2018). Chemical weathering rates generally increase as physical erosion rates increase (Riebe et al., 2004a) and remain elevated at high rates of physical erosion (Gabet and Mudd, 2009; Dixon and von Blanckenburg, 2012; West, 2012; Larsen et al., 2014). In steady-state mountain ranges, physical erosion rates are a function of rock uplift rates. However, knickpoint propagation can drive transient erosion, generating spatially variable physical erosion rates within (e.g., Hurst et al., 2012) or between (e.g., Willett et al., 2014) catchments, which causes variation in chemical weathering rates and weathering intensity. For example, in the rapidly eroding San Gabriel Mountains, chemical weathering intensity in soils is lower downstream from knickpoints relative to soils on hillslopes upstream from knickpoints where erosion rates have not yet responded to tectonically-driven increases in fluvial incision (Dixon et al., 2012). Hence weathering intensity decreases when soils thin and mineral residence times decline as hillslope topography responds to knickpoint propagation.

Measurements across altitudinal transects generally show that chemical weathering intensity and chemical weathering rates decline with increasing elevation, which has been attributed to the loss of vegetation and development of rocky hillslopes with little soil mantle (Drever and Zobrist, 1992; Riebe et al., 2004b) and decreasing temperature (Norton and von Blanckenburg, 2010; Dixon et al., 2009, 2012). For example, in the Swiss Alps, concentrations of dissolved cations and silica in surface waters decrease exponentially as vegetation changes from forest to unvegetated rock and talus (Drever and Zobrist, 1992). Similarly, chemical weathering rates in soils decline with increasing elevation from 24 $t\,km^{-2}\,yr^{-1}$ to 0 $t\,km^{-2}\,yr^{-1}$ in the Santa Rosa Mountains, Nevada, with the lowest rates at high, unvegetated alpine sites (Riebe et al., 2004b).

Although physical erosion rates and the abundance and type of vegetation have been identified as important controls on chemical weathering, few studies have examined the relative influence of these two factors on chemical weathering rates in the same setting. Here we focus on part of the Whataroa River catchment in the western Southern Alps of New Zealand. At our study site on Gunn Ridge, dense forest vegetation transitions to grassland, and then to unvegetated alpine hillslopes with increasing elevation, but drainage divide migration also drives an order-of-magnitude variability in catchment-averaged erosion rates. We use the cosmogenic nuclide ^{10}Be and geochemical mass balance to evaluate soil production (Heimsath et al., 1997) and chemical weathering rates (Riebe et al., 2004a) across the vegetation and erosion rate gradients to determine which of these drivers more strongly influences chemical weathering.

2. Study site

We collected soil and sediment samples within the Whataroa River catchment in the Southern Alps of New Zealand (Fig. 1). The Whataroa River drains the Southern Alps east of the Alpine Fault in an area where long-term exhumation rates are 8.7 ± 1.3 $mm\,yr^{-1}$ (Herman et al., 2010). ^{10}Be concentrations in river sediment indicate the catchment-averaged denudation rate is 6.6 ± 1.7 $mm\,yr^{-1}$ (Fig. 1; Larsen et al., 2014). Since the last glacial termination approximately 17,300 years ago (Barrows et al., 2013), the high rates of erosion, driven primarily by landsliding (Hovius et al., 1997) have transformed U-shaped glacier-carved valleys into V-shaped fluvial valleys (Prasicek et al., 2015).

We collected samples both to the north and south of the drainage divide on Gunn Ridge, which separates tributaries that drain to the mainstem Whataroa River (Fig. 1B). Gunn Ridge is located approximately 10 km south-east of the Alpine fault, in an area where provenance data based on metamorphic temperature suggest physical erosion rates in the Whataroa catchment are highest (Nibourel et al., 2015). The metamorphic grade of the Rakaia terrane schist at all sites is chlorite greenschist (GNS, 2022). The bedrock is foliated, which causes lithologic heterogeneity; the coefficient of variation (standard deviation/mean) in major oxide concentrations for elements that make up >1% of the rock mass ranges from 0.06 (SiO_2) to 0.36 for CaO, whereas the coefficient of variation for Zr is 0.15 (Table S1). The presence of large-scale retrogressive tension scarps on the eastern part of Gunn Ridge indicate part of the mountain is undergoing deep-seated gravitational failure (Korup, 2005), an interpretation supported by our field observations of slope failures with south-dipping failure planes (Figs. S1, S2).

Gridded data indicate the mean annual precipitation is 7400 $mm\,yr^{-1}$ at the sample sites (Ministry for the Environment and Statistics New Zealand, 2017). All the study sites are within the same 0.5 km resolution precipitation grid cell, but the distribution of vegetation on Gunn Ridge indicates the sites span strong environmental gradients. Vegetation type varies with elevation, with dense montane forests at low elevation, and tussock grassland vegetation that transitions to unvegetated rocky slopes at higher elevations (Fig. 2). Holocene vegetation in the western Southern Alps is thought to have responded to steady increases in summer temperature, with forests reaching their current elevation ~2500 yr BP (McGlone and Basher, 2012). Our samples from forest, tussock, and alpine ecosystems range in elevation from 550 to 910 m, 1440 to 1530 m, and 1740 to 1840 m, respectively. Below tree line, the mean forest biomass in the western Southern Alps is 3.5×10^4 $Mg\,km^{-2}$, which declines to zero for unvegetated, high-elevation sites (Hilton et al., 2011).

3. Methods

3.1. ^{10}Be and elemental geochemistry

We described soils, collected samples, and measured soil thickness at eight high-elevation soil pits located on ridgelines or on local-scale topographic convexities (Fig. 1C). Five of the sites were characterized by tussock grassland vegetation (pits 16–18, 20, 21). The three alpine sites had little to no vegetation (pits 8–10). Three of the sites were located on the north side of the drainage divide where the topography is low gradient (pits 8, 10, 18). Two of the sites north of the drainage divide were from the alpine ecosystem and were located close to the drainage divide (pits 8, 10), whereas the third site was from an area with tussock vegetation on the part of Gunn Ridge that displays evidence of deep-seated gravitational failure (pit 18). The other five sites were located on steep ridges to the south of the drainage divide; one in the alpine ecosystem (pit 9) and four in the tussock grassland (pits 16, 17, 20, 21) (Fig. 1C). The soils directly overlie fractured bedrock with minimal saprolite development (Eger et al., 2018). Sediment was collected for ^{10}Be analysis from a stream that drains the low-gradient area and flows north from the drainage divide to the mainstem Whataroa River. We also incorporated and re-analyzed published ^{10}Be data from seven soil pits south of the drainage divide, located in dense forest (pits 1-7), and one sediment sample from a watershed that drains southward to the mainstem Whataroa River (Larsen et al., 2014).

At sites with tussock vegetation, where soils are characterized by clast-rich AC and CR horizons (Table S2), we collected a composite sample that extended from the ground surface to the base of the soil, including large rock fragments within the soil. We also sampled fractured bedrock at the base of soil pits. The soil morphology of the alpine sites differed from the tussock sites and were characterized by a layer of tabular clasts of schist bedrock that covered the soil surface above a cumulate A-horizon, with a Bw horizon beneath (Table S2). The surface clasts most likely accumulated due to heave from below or frost cracking and spalling of nearby

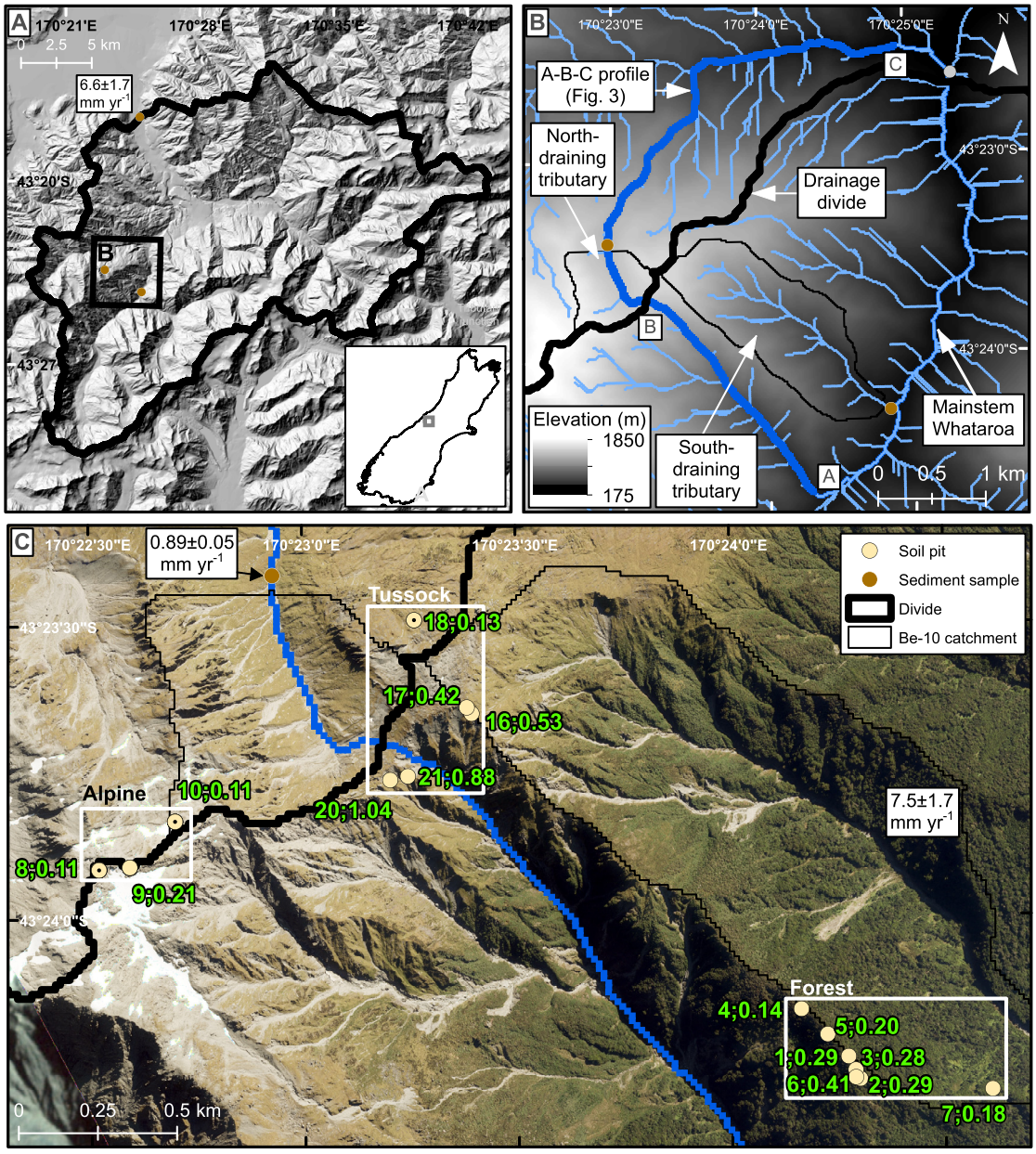

Fig. 1. Study site and sample locations. A) Hillshade map showing the location of the study site within the Whataroa River catchment on the South Island of New Zealand (inset). B) Digital elevation model showing the drainage divide (thick black line) and drainage network (blue lines) on Gunn Ridge. The thick blue line shows the A-B-C profile shown in Fig. 7. All the streams on Gunn Ridge drain to a common junction that we used for χ analysis, shown by the gray circle. The locations of sediment samples collected for watershed-scale ^{10}Be analysis are shown in brown circles and the watersheds are delineated with thin black lines. C) Aerial images (courtesy Land Information New Zealand) showing the locations of soil samples with respect to the drainage divide (thick black line) and vegetation type. Soil pit symbols with dots are north of the drainage divide, whereas those without dots are south of the divide. Boxes group samples collected from areas with similar vegetation. Soil pit numbers and soil production rates, with units of mm yr^{-1}, are shown separated by a semicolon adjacent to each sample location. Denudation rates measured for the two catchments (delineated with thin black lines) draining each side of the divide are shown in boxes with a solid white fill.

rock outcrops, which are more common in the alpine area than at lower elevation. A frost-related origin of the alpine soils is consistent with their ~1750–1850 m elevation range, which is within the altitudinal zone where temperatures in the Southern Alps are most conducive to frost cracking (Hales and Roering, 2005). Beneath this layer the cumulate A-horizon has most likely formed by infiltration of finer spalled material from above and from disintegration of the surface clasts, akin to the process described for Antarctic soils by Scarrow et al. (2014) (Fig. S3). The horizonation was most distinct at the two highest elevation alpine sites (pits 8 and 9) where we sampled the surficial clasts, each soil horizon, including rock fragments, and rock at the base of the pit. The horizonation was not as distinct at the lower elevation alpine site (pit 10), and we sampled the 40 cm-thick profile in two 20 cm intervals, in addition to rock on the ground surface and at the base of the soil. At all sites, we collected 500 mL of soil by driving a rectangular steel box into the pit walls and used the dry mass to determine bulk density.

We split dry soil samples using a riffle splitter with 1-cm openings. Rock fragments too large to pass through the splitter were reserved for separate analysis. We wet-sieved the soils to isolate the 250-850 µm grain-size fraction for ^{10}Be analysis. For the alpine soils, we also analyzed ^{10}Be in the surficial rock and the rock fragments within the soil and for two of the alpine sites (pits 8 and 9), we measured ^{10}Be in the rock from the base of the soil pit. We used standard methods to purify quartz (Kohl and Nishiizumi,

Fig. 2. Field photographs of the three ecosystems we sampled: A) largely unvegetated alpine, B) tussock grassland, C) temperate forest.

1992) and to dissolve the quartz and extract ^{10}Be (see Supplementary material for analytical details). ^{10}Be/^{9}Be ratios were measured at the Center for Accelerator Mass Spectrometry at Lawrence Livermore National Laboratory. Based on prior work (Larsen et al., 2014), we assume soils are vertically mixed, and that the surface ^{10}Be production rate is appropriate for calculating denudation, or soil production rates (Granger and Riebe, 2014). Soil production rates calculated from lower soil horizons and bedrock at the base of pits 8, 9, and 10 use a shielding correction based on the density and thickness of overlying soil (e.g., Heimsath et al., 1997). We do not correct for shielding by snow. We use a topographic shielding correction for each soil pit location but assume no topographic shielding when interpreting ^{10}Be concentrations in sediment collected from the watersheds (DiBiase, 2018). Production rate parameters were calculated for each soil pit and watershed using a 15 m digital elevation model (DEM) (Columbus et al., 2011) following Mudd et al. (2016). We used version 3 of the Balco et al. (2008) online calculator to determine denudation rates from the ^{10}Be concentrations (Table S3) and report internal 1 standard error (S.E.) uncertainties based on 'St' (Lal, 1991; Stone, 2000) production rate scaling. We calculated mineral residence time by dividing soil thickness by the denudation rate. In well-mixed soils such as those in the Southern Alps (Larsen et al., 2014), mineral residence times are equivalent to soil turnover-times, which describe the timescale of mineral depletion within the soil (Mudd and Yoo, 2010).

Major and trace element concentrations were measured on splits of soil samples, including both fine-grained material and coarse rock fragments (defined by material passing and not passing through the splitter, respectively), bedrock at the base of each pit, and, for the alpine sites, surficial rock clasts. The average dry sample weight was ~10 kg, and to obtain a representative sample, we typically processed one-eighth of the material for XRF measurements. The coarse and fine fractions of the one-eighth splits were separately pulverized in a jaw crusher and split again to generate ~100 g of representative material. The ~100 g splits were then milled to 100-200 mesh in a tungsten carbide shatterbox. Loss-on-ignition (LOI) was determined by heating ~2 g of sample to 850°C for 10 min.

Aliquots of the powdered sample were analyzed by X-ray fluorescence (XRF) spectroscopy. Major elements (Si, Ti, Al, Fe, Mg, Ca, Na, K, P) were measured as oxides on duplicate fused glass discs, prepared by fusing 0.6 g of sample with 6 g of a pre-fused Claisse Li-borate flux in an Eagon-2 automated fusion furnace. Prior to fusion the powders were pre-ignited at 850 °C for several hours to remove volatiles (H_2O, CO_2, S, etc.) and oxidize iron to Fe^{3+}. Analyses were conducted using a Panalytical Zetium spectrometer using Panalytical's WROXI synthetic standards and software. The standards are prepared from high purity chemicals and cover a wide range of compositions and are supplemented with a few extreme rock and mineral standards (e.g., Dunite (DTS-1); K- Feldspar (NBS-70a)). The predominant use of synthetic standards essentially makes these category-2 solution-based analyses (Jochum et al., 2015).

Trace elements (Rb, Sr, Nb, Zr, Y, U, Th, Pb, Zn, Ga, Ni, Cr, V) were measured on a Panalytical PW2400 spectrometer. The pellets were prepared from 10 g of un-ignited powders, mixed with a few drops of poly-vinyl alcohol solution, and pressed at 7 tons on a Spex hydraulic press. These pellets are of infinite thickness for the X-ray wavelengths of interest. The measured intensities were corrected for non-linear background, X-ray tube, and inter-element interferences, and variations in mass absorption coefficients of samples and standards, using methods modified from Norrish and Chappell (1967) and Chappell (1991). The principal difference is in the determination of mass absorption coefficients. Mass absorption coefficients for elements with measured characteristic wavelengths shorter than the Fe absorption edge (Ni, Zn, Ga, Pb, Th, Rb, Sr, Zr, Nb) are estimated from the inverse intensity of the Compton scattered radiation of the Rhodium X-ray tube (Reynolds, 1967; Willis, 1991). Mass absorption coefficients of elements with longer characteristic radiation than the Fe absorption edge (Cr, V) were calculated from the Rh Compton-derived mass absorption coefficients and intensities for Fe (Cr) and Ti (V) (Walker, 1973). Major element and Zr concentrations for samples first reported by Larsen et al. (2014) were measured via XRF by ALS Minerals, Vancouver, Canada (Table S4).

Replicate trace element measurements on three samples indicate the coefficient of variation in Zr concentrations ranged from 0.012 to 0.038 (Table S5). Since the uncertainty in the Zr concentrations is low and sample-dependent, likely due to variability in Zr content among samples (see Supplementary material), we do not propagate uncertainty in Zr concentrations into further analyses.

3.2. Analysis of ^{10}Be and geochemical data

^{10}Be concentrations reflect the denudation rate D, which is equivalent to the bedrock-to-mobile regolith, or soil production rate (SPR) if the soil thickness is constant in time (Heimsath et al., 1997):

$$SPR = D = W + E \tag{1}$$

where D reflects the sum of mass loss due to chemical weathering W and physical erosion E (Riebe et al., 2004a). D, W and E have units of M L^{-2} T^{-1}, and we convert the units to L T^{-1}, based on a measured bedrock density of 2.65 g cm^{-3} (Larsen et al., 2014). We calculated the chemical depletion fraction CDF, by assuming Zr is a chemically immobile element:

$$CDF = \left(1 - [\mathrm{Zr}]_{rock} / [\mathrm{Zr}]_{soil}\right) \tag{2}$$

where the terms in brackets are Zr concentrations measured in rock and soil. The CDF is equal to W/D, hence:

$$W = D \cdot \left(1 - [\mathrm{Zr}]_{rock} / [\mathrm{Zr}]_{soil}\right). \tag{3}$$

By substituting eq. (3) into eq. (1) to solve for E, values of D, W, and E were determined for each soil sample.

Zr concentrations can be non-uniform in the Alpine Schist (Larsen et al., 2014). Some of the bedrock at the base of the pits had Zr concentrations that exceeded that in the soil (Table S1), which was inconsistent with our field-based observations of the degree of weathering. Hence, we assumed that large rock fragments (those not passing through the riffle splitter), which on average, made up one-third of the mass of each soil sample, better characterize the parent material and use measurements in those clasts to characterize $[Zr]_{rock}$. We used the masses of the coarse rock fragments and the fine soil material, and their respective Zr concentrations to determine a weighted mean Zr concentration for the entire mobile regolith (fine and coarse soil fractions) at each site. The soil samples in the tussock and forest vegetated areas were organic-rich. To remove the effect of dilution by organic matter on measured concentrations, and hence calculate Zr concentrations in mineral soil only, we corrected all measured concentrations:

$$[Zr] = [Zr]_{measured} \cdot (100/(100 - LOI)) \tag{4}$$

where $[\mathrm{Zr}]_{measured}$ is the measured Zr concentration in the unignited pressed pellet. Experiments conducted on three samples (see Supplementary material for details) indicate Zr concentrations calculated via eq. (4) are statistically indistinct from those measured in samples that were ignited prior to pressing the pellets (Table S5).

For all samples, we assessed relationships between soil production rate and soil thickness, CDF and soil thickness, CDF and soil production rate, and CDF and residence time (Table S6). We also tested for differences in soil production rate, chemical weathering rate, physical erosion rate, and CDF as a function of location with respect to the drainage divide (north versus south) and vegetation type. A Shapiro-Wilks test indicated that some of the data classified by location with respect to the drainage divide were normally distributed, whereas others were not (Table S7). Hence, we used a t-test and a non-parametric Mann-Whitney U test to evaluate cross-divide differences. Since both tests yielded consistent results as to whether there were significant differences (using a p-value of 0.05), we report the t-test results here and the results of both tests in Table S7. The Shapiro-Wilks test indicated most datasets classified by vegetation type were normally distributed (Table S8), hence we used a one-way ANOVA to evaluate whether values differed as a function of the three vegetation types and the *post-hoc* Tukey HSD test to assess pairwise differences. The challenging nature of fieldwork in the Southern Alps limited the number of samples we collected. Though assessment of statistical power is typically done *a priori*, rather than *post-hoc*, we estimate that the statistical power of the comparisons of soil production rate, chemical weathering rate, physical erosion rates, and CDF across vegetation and with respect to the drainage divide are on the order of 0.48–0.65 and 0.38–0.51, respectively (see Supplementary material for details).

3.3. Topographic analysis

We conducted several analyses on DEMs with different resolutions to place the geochemical measurements within their geomorphic context. We used LSDTopoTools (Mudd et al., 2014) to analyze river long profiles using the integral method (Perron and Royden, 2013) to measure χ and used the gradient in χ to assess channel steepness. Cross-divide differences in river profile metrics were used to assess drainage divide migration potential (e.g., Willett et al., 2014).

We also measured valley convexity to assess whether the valley north of the divide retains relict glacial topography that has not yet responded to tectonically-driven changes in base level. Normalized cross-sectional curvature values for valley bottom DEM grid cells measured over multiple spatial scales quantify differences in valley concavity (Prasicek et al., 2014). Minima in the absolute value of curvature, which occur in the most concave portions of valley cross-section profiles, occur at smaller spatial scales for V-shaped cross-sections, relative to U-shaped cross-sections (Prasicek et al., 2014). The spatial scale at which minima in the absolute value of curvature occurs therefore provides a relative metric that can be used to assess whether a valley has a fluvial V-shape, or a glacial U-shape. We calculated multi-scale curvature for two adjacent valleys on each side of the drainage divide and use the minimum curvature scale to differentiate between fluvial and glacial valley shapes. We used a 15 m resolution DEM (Columbus et al., 2011) to calculate channel and valley metrics, which is a suitable resolution (e.g., Wobus et al., 2006; Prasicek et al., 2014).

We generated a structure-from-motion (SfM) DEM with 0.5 m grid cell resolution using historical aerial photographs and Agisoft Metashape for the part of Gunn Ridge we sampled. We used the SfM-derived DEM to calculate slope angles and local relief using a moving circle with a 50-cell radius. We calculated mean slope and relief for 250 m wide buffer on either side of the drainage divide (Fig. S4) to assess potential for divide mobility (e.g., Forte and Whipple, 2018).

We smoothed the SfM-generated DEM with a two-dimensional gaussian filter with a full-width, half-maximum window size of 5 m, equivalent to 10 grid cells (Price-Whelan et al., 2018) and calculated curvature C (m^{-1}) using a second-order central difference approximation of the second derivative of elevation z (m):

$$C = \frac{z_{i+1,j} - 2z_{i,j} + z_{i-1,j}}{\Delta x^2} + \frac{z_{i,j+1} - 2z + z_{i,j-1}}{\Delta y^2} \tag{5}$$

where i and j are indices, Δx and Δy are grid cell sizes. Curvature was calculated for a surface constructed over a 5-cell window. However, we also tested different combinations of smoothing windows ranging from 0 to 12.5 m and curvature constructed over surfaces of 3, 5, 7, and 9 cells; results from those combinations are shown in Table S9. We used regression to assess the correlation between curvature and soil production rate and the correlation between curvature and soil thickness. The correlation between curvature and soil production rate and curvature and soil thickness is relatively similar for smoothing windows between 4 and 7.5 m,

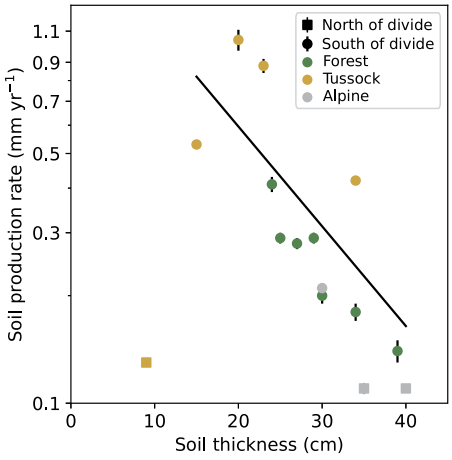

Fig. 3. The soil production function for Gunn Ridge. An exponential fit to the data with soil thickness >9 cm (i.e., excluding the data from Gunn Pit 18) with the form y=a*exp(−b*x) yields parameters a=2.15±1.09 mm yr^{-1} and b=-0.064±0.021, with $R^2 = 0.51$ and p=0.004.

hence we adopted a 5 m window size, as the correlation degrades for both larger and smaller smoothing windows due to scale effects (Fig. S5). Only the alpine and tussock samples were used for the curvature analysis because the SfM-derived DEM captures the tree canopy surface, rather than the ground surface, in the forested portion of the study area. Due to imperfect orthorectification of the SfM-derived DEM, GPS coordinates of some sample locations did not align exactly upon the ridgeline from which they were collected, and we manually adjusted the points to the correct locations. Because the data from pit 18 do not conform to the soil production function defined by data from all of the other sites, we omitted those data from the curvature analysis.

4. Results

Soil production rates on Gunn Ridge range from 0.110±0.004 to 1.04±0.07 mm yr^{-1} (Fig. 3; Table S6). Soil production rates decline exponentially as soils thicken (Fig. 3). Data from pit 18, where the soil thickness is 9 cm, do not follow the trend defined by the other sites. Pit 18 is on a large rock block within the area undergoing deep-seated gravitational failure, and is possible that the soil thickness and the soil production rates are out of equilibrium due to movement of the block. ^{10}Be concentrations indicate the alpine soils are vertically mixed and that soil production rates are uniform across grain sizes (Fig. S6). The *CDF* increases with soil thickness, generally declines as soil production rates increase, and increases with mineral residence time (Fig. 4).

The mean soil production, chemical weathering, and physical erosion rates are 2-3 times higher on the south versus the north side of the drainage divide and the differences between the two groups are significant (p=0.003 to 0.006) (Fig. 5; Tables 1, S7, S10). Mean *CDF* values are 0.14 north of the divide and 0.13 south of the divide, and these values are not significantly different (p=0.51).

When grouped by vegetation, soil production, chemical weathering, and physical erosion rates are always highest for the tussock grassland, relative to the forest and alpine ecosystems (Fig. 6; Tables 1, S8, S11). ANOVA analysis indicated there are significant differences in soil production, chemical weathering, and physical erosion rates as a function of vegetation type, but the *post-hoc* comparison indicates this is always due to differences between the tussock and another vegetation type (Table S12). The *post-hoc* analysis indicates there are not significant differences in soil production, chemical weathering, or physical erosion rates between the alpine and forest ecosystems, where the differences in biomass

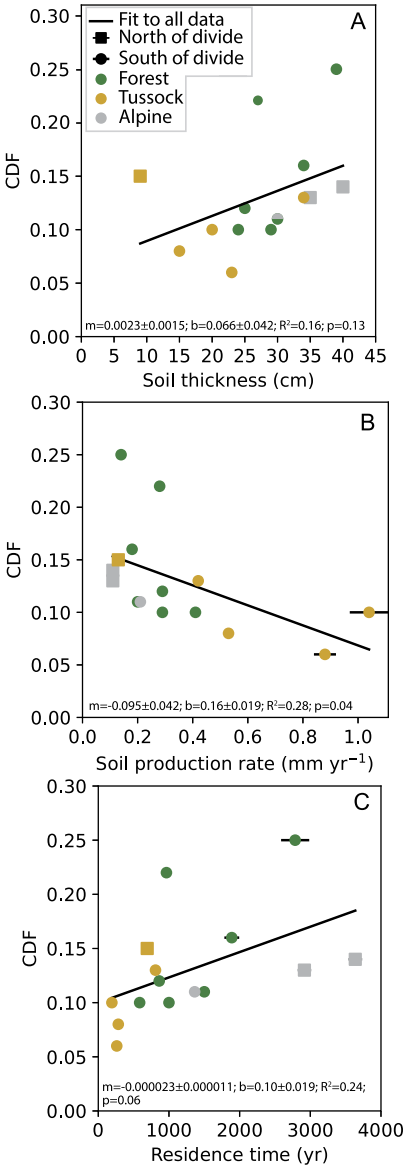

Fig. 4. A) CDF versus soil thickness; B) CDF versus soil production rate; C) CDF versus mineral residence or soil turnover time. Values for Gunn Pits 8, 9, and 10 are averages based on measurements from all depth increments. The coefficients for the linear regression (y=mx+b; m=slope; b=intercept), the correlation coefficient (R^2), and p-value are shown for fits to all data.

are greatest. Mean *CDF* values for the forest, tussock, and alpine ecosystems do not differ as a function of vegetation type (p=0.28).

^{10}Be concentrations indicate the denudation rate for the catchment draining south from the divide is 7.5±1.7 mm yr^{-1}; the denudation rate of 0.89±0.05 mm yr^{-1} for the north-draining catchment is nearly an order of magnitude lower (Figs. 1C, 7D). Channel steepness data indicate that near the drainage divide, south-draining channels are steeper than those that drain to the north (Fig. 7A). A plot of elevation versus χ for streams draining each side of the drainage divide indicates χ values at the divide are greater on the north versus south draining streams (Fig. 7F). Hillslope angles and local relief in the south-draining tributary are greater than in the north-draining tributary (Figs. 7B, S4). However, the distribution of steep versus more gentle topography does not coincide exactly with the drainage divide, as there are areas with low slope and relief directly adjacent to the south side of the divide (Fig. 7B, S4). The valley shape analysis indicates minimum normalized curvature window size is elevated, relative to adjacent

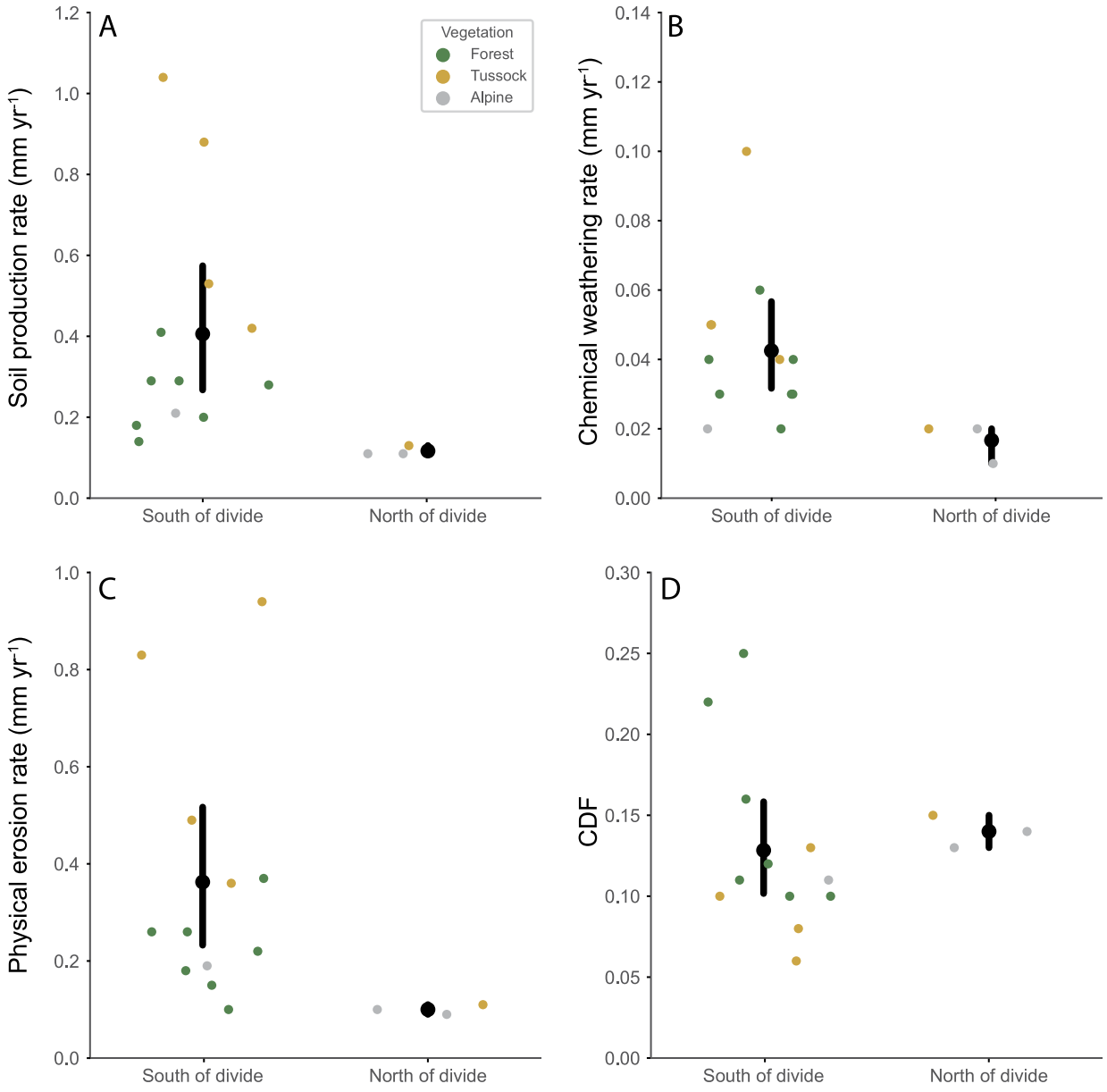

Fig. 5. Cross-drainage divide differences in: A) soil production rate, B) chemical weathering rate, C) physical erosion rate, and D) CDF values. Black circles show the mean, lines show 95% confidence intervals, and circles show values of individual measurements, colored by vegetation type.

valley segments, over a ~1 km-long portion of the north draining valley adjacent to the drainage divide (Fig. 7E), which indicates there is a U-shaped glacial valley segment in the headwaters of the north-draining tributary (Prasicek et al., 2014).

Ridgetops are generally more convex (curvature values are more negative) to the south versus the north of the migrating divide (Figs. 7C, S4). For the alpine and tussock sites (excluding data from pit 18), soil thickness declines as ridges become more convex (Fig. 8A). For the same sites, soil production rates increase as topographic convexity increases (Fig. 8B). Our results from Gunn Ridge follow the same trend defined by a compilation of catchment-averaged ^{10}Be and ridgeline curvature data from across the United States (Gabet et al., 2021). There is an approximately square-root relationship between denudation rate and curvature (Fig. 8C; Gabet et al., 2021), although the specific square-root relationship may be a scaling artefact caused by under-estimation of curvature in highly convex terrain (Strubble and Roering, 2021).

5. Discussion

5.1. Evidence for drainage divide migration at Gunn Ridge

The higher channel steepness, greater hillslope angles and local relief, and lower χ values to the south versus the north of the drainage divide are topographic signatures of northward drainage divide migration on Gunn Ridge (e.g., Willett et al., 2014; Forte and Whipple, 2018) and are consistent with the near order-of-magnitude difference in cross-divide catchment-averaged denudation rates. Valley shape analysis and field observations (Fig. S7) indicate divide migration is occurring by headward fluvial incision into the remnant topography of a glacially carved landscape that has lower erosion rates. The field observations, catchment-scale denudation rates, and topographic analyses hence demonstrate some of our soil samples are from a relict glacially carved landscape that has yet to respond to base-level change, whereas others are from hillslopes that have responded to base-level change and are eroding at higher rates.

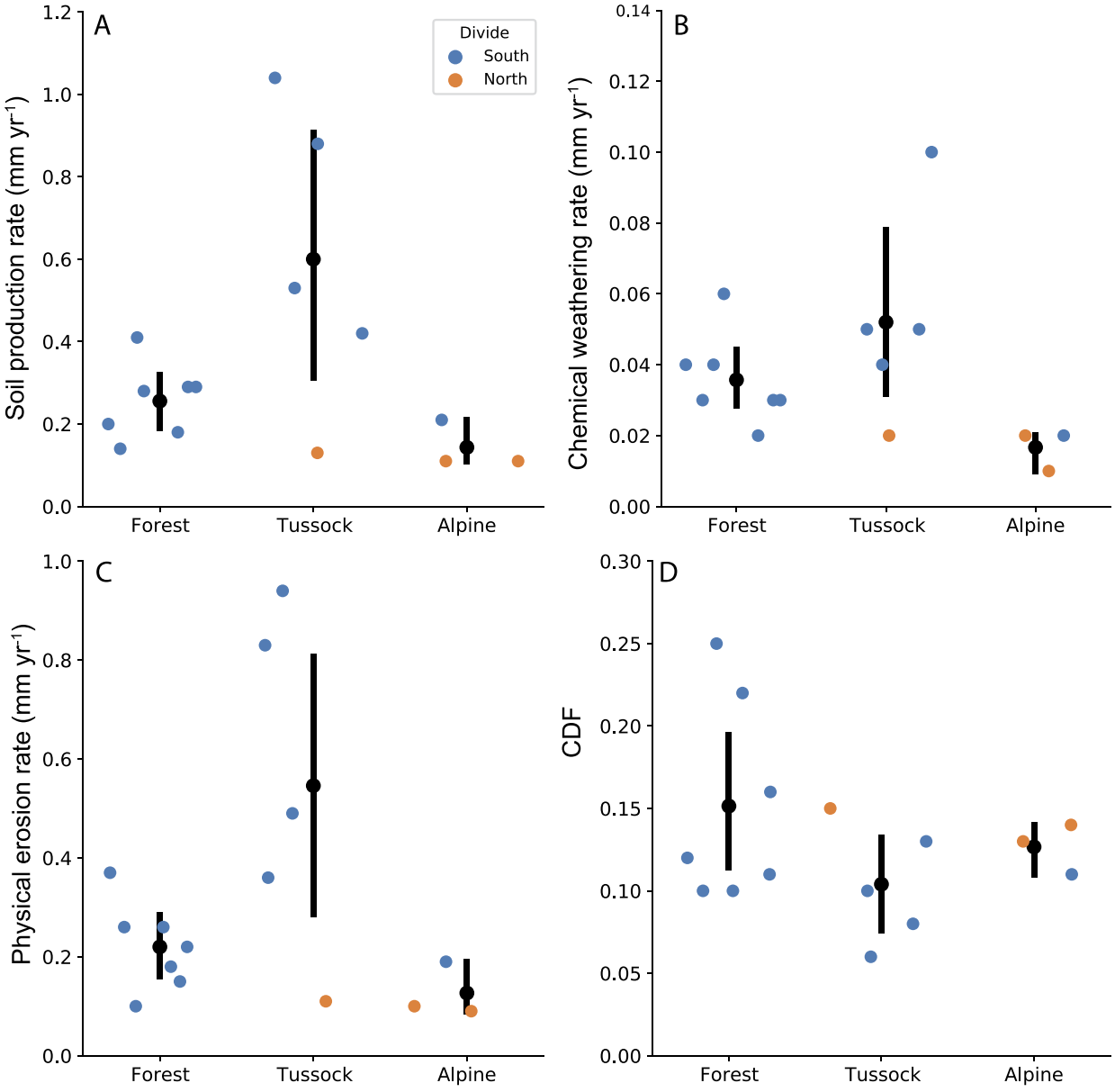

Fig. 6. Differences in: A) soil production rate, B) chemical weathering rate, C) physical erosion rate, and D) CDF values for samples from forest, tussock, and alpine ecosystems. Black circles show the mean, lines show 95% confidence intervals, and circles show values of individual measurements, colored by location with respect to the drainage divide.

5.2. The relative influences of erosion and vegetation on soil production and weathering rates

The high soil production rates on Gunn Ridge, relative to other landscapes (e.g., Larsen et al., 2014), may arise largely due to the exceptional convexity of ridgetops in the western Southern Alps relative to other settings (Fig. 8C). Measurements of ridgetop curvature provide a mechanistic link between the observed spatial pattern of fluvial incision and soil production rates. Ridgetops are more convex in the rapidly eroding landscape south of the drainage divide than in the more slowly eroding landscape to the north. Soil production rates increase as ridgetop convexity increases, indicating soil production rates are responding to fluvial incision rates. These findings are consistent with the conclusion of Heimsath et al. (2012), who indicated that soil production rates increase with catchment scale denudation rates. However, we note that the maximum soil production rate measured in the western Southern Alps is much lower than catchment-averaged denudation rates, implying other mechanisms of denudation, such as landsliding, also initiate in response to increased relief generation.

Relative rates of fluvial incision control the distribution of soil production and weathering rates on Gunn Ridge, but bedrock strength may also influence the overall magnitude of the soil production rates we measure. Rock fracturing influences the extent of soil cover (Neely et al., 2019). Near-surface bedrock in the Southern Alps is extensively fractured due to tectonics (Clarke and Burbank, 2011), which may explain why the western Southern Alps maintain a soil mantle despite high erosion rates (Neely et al., 2019). Rock damage due to topographic stresses is predicted to increase with topographic convexity (Moon et al., 2017), which may further weaken bedrock on ridgetops. Given that bedrock is converted to soil by abiotic and biotic disturbances at the soil-bedrock interface (e.g., Heimsath et al., 1997), such as frost cracking (e.g., Hales and Roering, 2005) or root growth (e.g., Larsen et al., 2014), soil production rates may be faster where rock is fractured if the weaker rock permits a greater degree of soil production per disturbance. Bedrock fracturing may also explain why chemical weather-

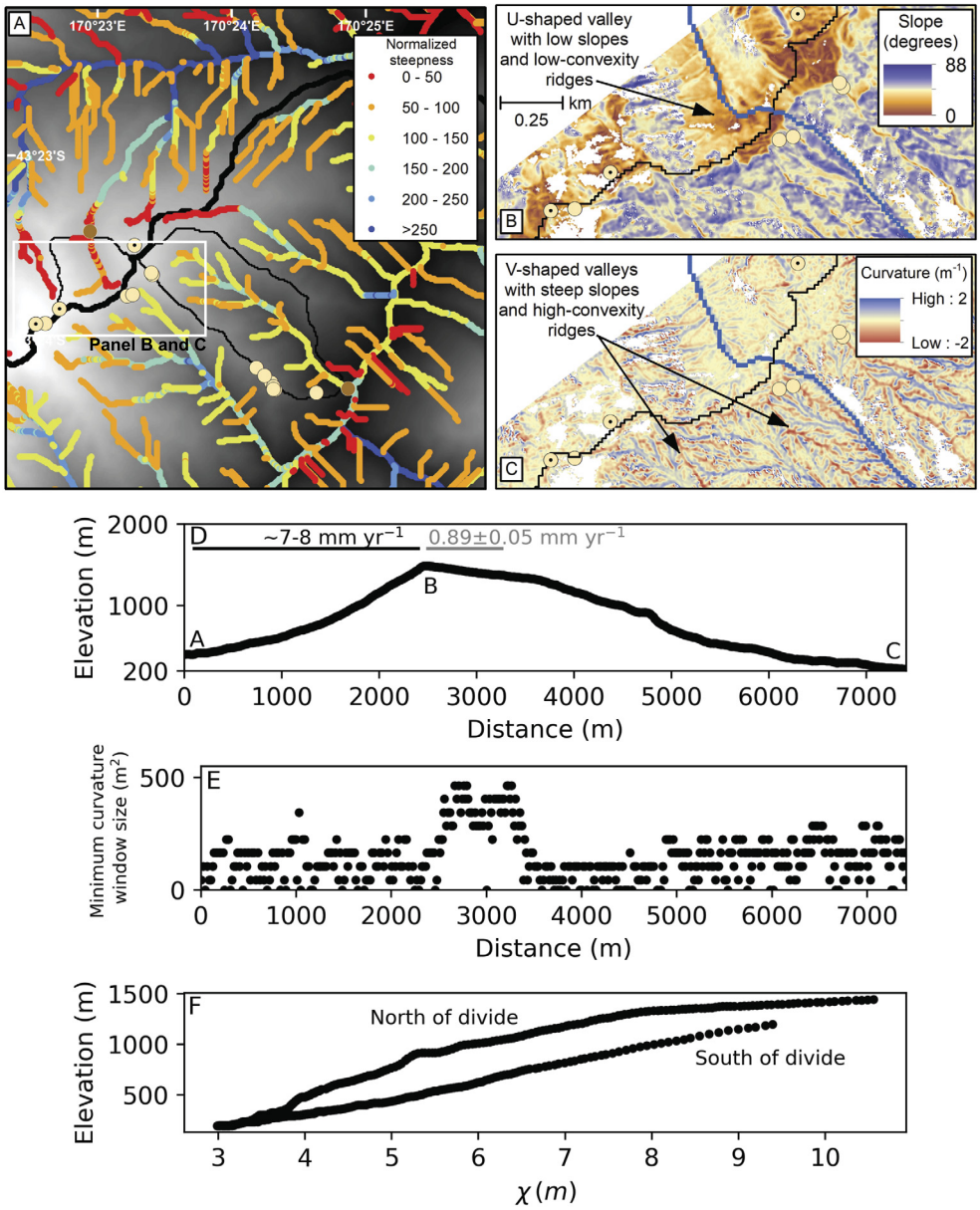

Fig. 7. A) Map of channel steepness for streams draining each side of Gunn Ridge. B) Slope map and C) topographic curvature map calculated from a structure-from-motion digital elevation model. D) Topographic profile that crosses Gunn Ridge from south to north along the A-B-C profile in Fig. 1B. The denudation rate of the south-draining channel is approximately 7-8 mm yr^{-1}, based on ^{10}Be measurements in the adjacent watershed, whereas the denudation rate in the low-gradient, high elevation portion of the watershed north of the divide is 0.89±0.05 mm yr^{-1}. E) Minimum curvature window size (m^2) along the topographic profile shown in D. The increase in window size centered on distance ≈3000 m is diagnostic of U-shaped glacial topography, whereas the lower values to the north and south are diagnostic of V-shaped, fluvially-incised valleys. F) χ-plots for two streams draining north (from B to A along the profile shown in panel D) and south (from B to C) on Gunn Ridge demonstrate χ-values at the divide are greater for the north-draining stream, which is indicative of northward drainage divide migration.

ing rates in the alpine ecosystem are relatively high, even in the absence of vegetation, as fracturing may permit extensive contact between fresh minerals and rapidly flushed fluids (e.g., Maher and Chamberlain, 2014) in this high-rainfall environment.

The *CDF* values for the forest and alpine ecosystems, where the differences in vegetation biomass and productivity are expected to generate the strongest contrast in weathering intensity, are not significantly different. Additionally, the highest soil production rates on Gunn Ridge occur in the tussock grassland ecosystem, rather than the forest, which indicates plant biomass is not the dominant driver of soil production in this setting. Most of the tussock grassland sites are located just in the wake of the migrating drainage divide. Qualitative field observations indicate the ridges at the tussock sites are more convex than the forested ridges we sampled and that the drainage density is greater in the tussock ecosystem. The reasons for these observations are unclear, but the higher drainage density may be influenced by increased surface runoff above treeline and the lack of cohesive strength imparted by tree roots. It is also possible that the lower convexity of hilltops in the forest reflects adjustment to the passage of a knickzone (e.g., Hurst et al., 2013) and that the highest rates of fluvial incision are currently focused near the divide at the elevation of the tussock grassland. Regardless of the cause of the differences in curvature between the tussock and forest sites, the high convexity of the ridges for both the tussock and alpine sites south of the drainage divide, relative to the lower convexity ridges to the north, indicate the topography, and hence soil thickness, soil production rates, and mineral residence times, are responding to high rates of fluvial incision. Hence the higher soil production and chemical weathering rates in the tussock ecosystem relative to the forest ecosystem are

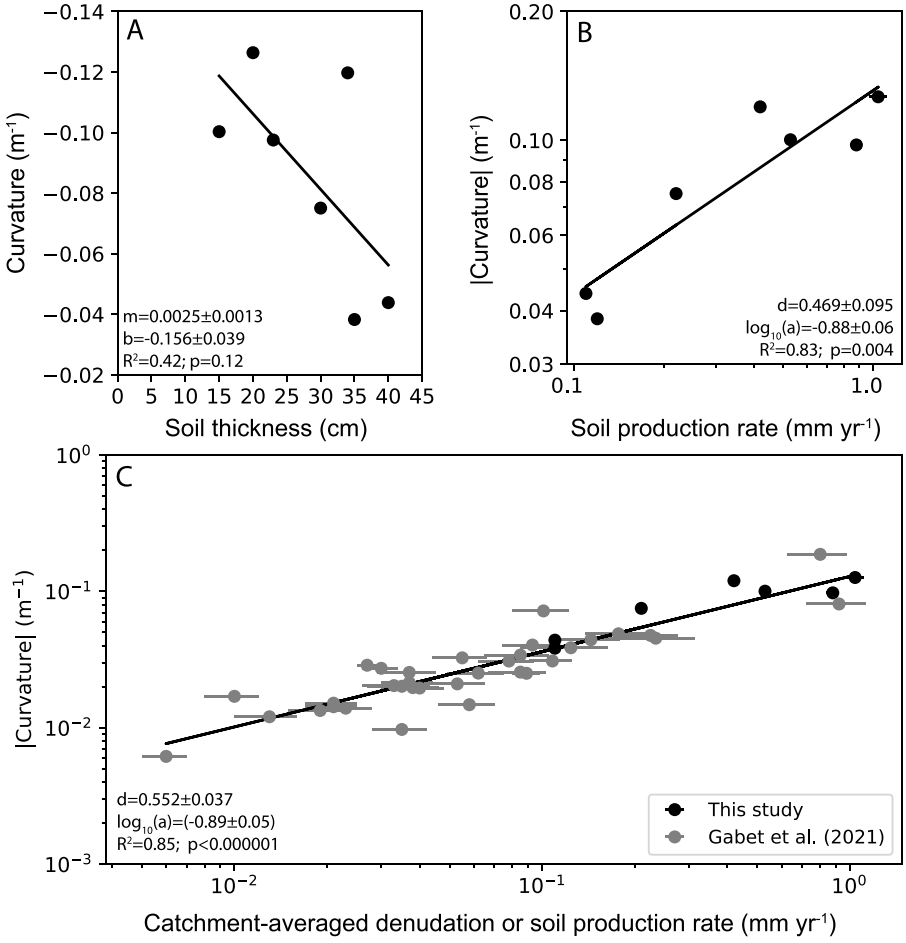

Fig. 8. Relationships between: A) topographic curvature and soil thickness, B) the absolute value of topographic curvature and soil production rate, and C) the absolute value of topographic curvature and soil production rate (this study) or catchment-averaged denudation rate (Gabet et al., 2021). The coefficients for the linear regression fit in A (y=mx+b; m=slope; b=intercept) and the power law fits in B and C (y=ax^d; d=power-law exponent; a=intercept), correlation coefficient (R^2), and p-value are shown.

primarily driven by hillslope response to base level fall, rather than differences in vegetation. However, we do not suggest that vegetation plays no role in the physical and chemical conversion of bedrock to soil in the Southern Alps. Unlike the soils in the alpine and tussock ecosystems, the forest soils we sampled often exhibited incipient podsolization (Table S2), suggesting that the forest favors increased chemical differentiation beyond that simply related to soil residence time. Observations of tree root growth in fractures also suggests vegetation plays a role in the conversion of soil to bedrock (Larsen et al., 2014). However, the influence of vegetation on soil production and chemical weathering rates is apparently overwhelmed by the order of magnitude variability in landscape-scale erosion rates that control topography, soil thickness, and mineral residence times in this setting. Even if our sample size is too small to detect a statistically significant influence of vegetation, if such an influence exists, our results suggest it is relatively small.

There is an expectation that rock damage by frost, roots, topographic stresses, and other factors contribute to soil production. However, it is difficult to empirically untangle the relative contributions of these factors. Though development of models that simulate the influence of tree throw (e.g., Gabet and Mudd, 2010) and frost cracking (e.g., Anderson et al., 2013) have advanced understanding of the conversion of bedrock to soil, more work is needed to elucidate the mechanistic details of soil production. Whereas some studies show clear vegetative or altitudinal controls on chemical weathering (Drever and Zobrist, 1992; Riebe et al., 2004b), our work, and other recent studies based on samples that span larger environmental gradients have drawn more nuanced conclusions. For example, measurements from soils across an environmental gradient in Chile show that chemical weathering rates first increase and then decline as vegetation increases (Schaller and Ehlers, 2022). Further, at three sites spanning a wide range of erosion rates, chemical weathering rates are not controlled by biomass growth, but weathering intensity is instead a function of soil or regolith residence time (von Blanckenburg et al., 2021). With increasing vegetation, nutrient recycling and secondary mineral formation can lead to a reduction in regolith weathering (Oeser and von Blanckenburg, 2020). Hence, there may be a variety of reasons that explain why chemical weathering rates do not scale monotonically with vegetation abundance in some settings.

5.3. Implications for silicate weathering in the western Southern Alps

The load of the Whataroa River and other rivers draining the western Southern Alps is dominated by suspended sediment (Jacobson et al., 2003; Jacobson and Blum, 2003), which indicates the catchment-averaged denudation rates we measure primarily reflect physical erosion. Landsliding is the dominant agent of hillslope erosion in the western Southern Alps (Hovius et al., 1997), as soil production rates are <10% of landslide erosion rates and catchment-averaged denudation rates (Larsen et al., 2014). Despite the high ratio of physical erosion to chemical weathering, the flux of dissolved solids from these rivers is exceptionally high relative to rivers worldwide. The high solute export from the western Southern Alps is driven predominantly by Ca derived from car-

Table 1
Mean and standard deviation of soil production rates, chemical weathering rates, physical erosion rates, and chemical depletion fractions as a function of location relative to the drainage divide and vegetation type.

	Mean ($mm\,yr^{-1}$)	Standard deviation ($mm\,yr^{-1}$)
Location relative to drainage divide		
North of divide		
Soil production rate	0.12	0.01
Chemical weathering rate	0.017	0.005
Physical erosion rate	0.10	0.01
Chemical depletion fraction	0.14	0.01
South of divide		
Soil production rate	0.41	0.27
Chemical weathering rate	0.043	0.021
Physical erosion rate	0.36	0.26
Chemical depletion fraction	0.13	0.05
Vegetation type		
Forest		
Soil production rate	0.26	0.08
Chemical weathering rate	0.04	0.01
Physical erosion rate	0.22	0.08
Chemical depletion fraction	0.15	0.06
Tussock		
Soil production rate	0.60	0.33
Chemical weathering rate	0.052	0.026
Physical erosion rate	0.55	0.30
Chemical depletion fraction	0.10	0.03
Alpine		
Soil production rate	0.14	0.05
Chemical weathering rate	0.017	0.005
Physical erosion rate	0.13	0.04
Chemical depletion fraction	0.13	0.01

bonate weathering, but silicate chemical weathering rates inferred from solute flux data are still ~1.5 times greater than the global average (Jacobson and Blum, 2003).

Chemical weathering of landslide deposits is an important source of solutes delivered to rivers in the western Southern Alps, and this is primarily due to chemical weathering of trace amounts of carbonate within landslide deposits (Emberson et al., 2016). Bedrock in the western Southern Alps contains a small fraction (~0.002) of highly reactive hydrothermal calcite (Jacobson et al., 2003). Given that the *CDF* values we measure are orders of magnitude higher than the carbonate fraction, the chemical weathering that occurs when bedrock is converted to soil is dominated by dissolution of silicate minerals (e.g., Dixon and von Blanckenburg, 2012). Therefore, whereas landslide deposits are the source of the high carbonate-derived Ca weathering flux, soils are likely the locus of silicate weathering reactions in the Whataroa River catchment. Hence, although the potential for interaction between uplift rates and silicate weathering in the western Southern Alps is limited (e.g., Jacobson and Blum, 2003), soil-mantled hillslopes constitute the portion of the landscape where chemical weathering influences CO_2 drawdown. Our findings demonstrate that the soil mantle in the western Southern Alps is extensive and extends above treeline into the alpine zone. If generalizable to other uplifting mountain ranges, the finding that silicate weathering is focused on soil-mantled hillslopes highlights the importance of understanding how climate, vegetation, topography, and erosion rates interact to influence the distribution and persistence of soils, and of quantifying the chemical weathering rates from those soils, to constrain long-term silicate weathering rates.

6. Conclusions

Concentration of *in situ*-produced ^{10}Be and geochemical mass balance measurements for soils collected on Gunn Ridge in the Southern Alps of New Zealand indicate soil production and chemical weathering rates are controlled primarily by landscape-scale erosion rates, rather than vegetation. Topographic analyses and catchment-averaged ^{10}Be data indicate differential erosion is driving drainage divide migration on Gunn Ridge. Northward migration of the drainage divide is eroding a relict glacial valley that has not fully responded to base-level driven incision. Chemical depletion fractions are not significantly different for the rapidly-eroding landscape south of the divide and the slowly eroding landscape north of the divide, but soil production rates and chemical weathering rates are significantly higher within the rapidly eroding landscape. Soil production rates increase, and soil thickness decreases with increasing ridgetop convexity, and ridges are more convex south of the drainage divide where erosion rates are high. Our findings indicate that base-level driven fluvial incision propagates up hillslopes, leading to adjustments in ridgetop curvature, soil thickness, and soil production rates. Although the samples also span a vegetation gradient that includes temperate rainforest, tussock grassland, and unvegetated alpine ecosystems, chemical weathering intensity does not differ significantly as a function of vegetation. Nor does the forest ecosystem have the highest chemical weathering rates, as would be expected based on differences in ecosystem productivity. Hence chemical weathering rates at Gunn Ridge are controlled primarily by soil mineral residence times, which are in turn governed by physical erosion rates. The influence of vegetation on chemical weathering rates is overwhelmed by the role of erosion, such that a signature of vegetation on chemical weathering is not readily detectable in the rapidly eroding landscape of the western Southern Alps.

CRediT authorship contribution statement

Isaac J. Larsen: Conceptualization, Formal analysis, Investigation, Methodology, Writing – original draft. **Andre Eger:** Conceptualization, Formal analysis, Investigation, Methodology, Writing – review & editing. **Peter C. Almond:** Conceptualization, Investigation, Methodology, Writing – review & editing. **Evan A. Thaler:** Formal analysis, Investigation, Methodology, Writing – review & editing. **J. Michael Rhodes:** Formal analysis, Investigation, Methodology, Writing – review & editing. **Günther Prasicek:** Investigation, Methodology, Writing – review & editing.

Declaration of competing interest

The authors declare that they have no known competing financial interests or personal relationships that could have appeared to influence the work reported in this paper.

Data availability

All data are included as supplementary material and will be placed in a university library data repository.

Acknowledgements

This research was supported by the University of Massachusetts, Manaaki Whenua-Landcare Research, and NSF grant OISE-1015454 to Larsen. We thank Bob Newton and Marc Anderson at Smith College for assistance with ICP-OES measurements, Mike Vollinger for assistance with XRF analyses, Sean Willett for helpful discussions regarding drainage divide migration, and Cliff Riebe and two anonymous reviewers for constructive reviews. The historical aerial images were provided courtesy of the Retrolens Historical Image Resource (http://retrolens.nz). Geochemical and topographic data are available in the University of Massachusetts Scholarworks archive (https://doi.org/10.7275/ssgg-rp65).

Appendix A. Supplementary material

Supplementary material related to this article can be found online at https://doi.org/10.1016/j.epsl.2023.118036.

References

Almond, P., Roering, J., Hales, T.C., 2007. Using soil residence time to delineate spatial and temporal patterns of transient landscape response. J. Geophys. Res., Earth Surf. 112 (F3). https://doi.org/10.1029/2006JF000568.

Anderson, R.S., Anderson, S.P., Tucker, G.E., 2013. Rock damage and regolith transport by frost: an example of climate modulation of the geomorphology of the critical zone. Earth Surf. Process. Landf. 39, 299–316.

Balco, G., Stone, J.O., Lifton, N.A., Dunai, T.J., 2008. A complete and easily accessible means of calculating surface exposure ages or erosion rates from ^{10}Be and ^{26}Al measurements. Quat. Geochronol. 3, 174–195.

Barrows, T.T., Almond, P., Rose, R., Fifield, L.K., Mills, S.C., Tims, S.G., 2013. Late Pleistocene glacial stratigraphy of the Kumara-Moana region, west coast of South Island, New Zealand. Quat. Sci. Rev. 74, 139–159.

Berner, R.A., 1990. Atmospheric carbon dioxide levels over Phanerozoic time. Science 249 (4975), 1382–1386.

Chappell, B.W., 1991. Trace element analysis of rocks by X-ray spectrometry. In: Barren, et al. (Eds.), Advances in X-ray Analysis 34. Plenum Press, New York, pp. 263–276.

Clarke, B.A., Burbank, D.W., 2011. Quantifying bedrock-fracture patterns within the shallow subsurface: implications for rock mass strength, bedrock landslides, and erodibility. J. Geophys. Res., Earth Surf. 116 (F4). https://doi.org/10.1029/2011JF001987.

Cochran, M.F., Berner, R.A., 1996. Promotion of chemical weathering by higher plants: field observations on Hawaiian basalts. Chem. Geol. 132, 71–77.

Columbus, J., Sirguey, P., Tenzer, R., 2011. A free, fully assessed 15-m DEM for New Zealand. Surv. Q. 66, 16–19.

DiBiase, R.A., 2018. Increasing vertical attenuation length of cosmogenic nuclide production on steep slopes negates topographic shielding corrections for catchment erosion rates. Earth Surf. Dyn. 6, 923–931.

Dixon, J.L., Heimsath, A.M., Amundson, R., 2009. The critical role of climate and saprolite weathering in landscape evolution. Earth Surf. Process. Landf. 34, 1507–1521.

Dixon, J.L., Hartshorn, A.S., Heimsath, A.M., DiBiase, R.A., Whipple, K.X., 2012. Chemical weathering response to tectonic forcing: a soils perspective from the San Gabriel Mountains, California. Earth Planet. Sci. Lett. 323, 40–49.

Dixon, J.L., von Blanckenburg, F., 2012. Soils as pacemakers and limiters of global silicate weathering. C. R. Geosci. 344, 597–609.

Drever, J.I., Zobrist, J., 1992. Chemical weathering of silicate rocks as a function of elevation in the southern Swiss Alps. Geochim. Cosmochim. Acta 56, 3209–3216.

Drever, J.I., 1994. The effect of land plants on weathering rates of silicate minerals. Geochim. Cosmochim. Acta 58, 2325–2332.

Eger, A., Yoo, K., Almond, P.C., Boitt, G., Larsen, I.J., Condron, L.M., Wang, X., Mudd, S.M., 2018. Does soil erosion rejuvenate the soil phosphorus inventory? Geoderma 332, 45–59.

Emberson, R., Hovius, N., Galy, A., Marc, O., 2016. Chemical weathering in active mountain belts controlled by stochastic bedrock landsliding. Nat. Geosci. 9, 42–45. https://doi.org/10.1038/ngeo2600.

Forte, A.M., Whipple, K.X., 2018. Criteria and tools for determining drainage divide stability. Earth Planet. Sci. Lett. 493, 102–117.

Gabet, E.J., Mudd, S.M., 2009. A theoretical model coupling chemical weathering rates with denudation rates. Geology 37, 151–154.

Gabet, E.J., Mudd, S.M., 2010. Bedrock erosion by root fracture and tree throw: a coupled biogeomorphic model to explore the humped soil production function and the persistence of hillslope soils. J. Geophys. Res., Earth Surf. 115, F04005.

Gabet, E.J., Mudd, S.M., Wood, R.W., Grieve, S.W.D., Binnie, S.A., Dunai, T.J., 2021. Hilltop curvature increases with the square root of erosion rate. J. Geophys. Res., Earth Surf. 126. https://doi.org/10.1029/2020JF005858.

GNS Science, 2022. 1:250,000 scale Geological Map of New Zealand. https://data.gns.cri.nz/geology/. (Accessed 26 May 2022).

Granger, D.E., Riebe, C.S., 2014. Cosmogenic nuclides in weathering and erosion. In: Holland, H.D., Turekian, K.K. (Eds.), Treatise on Geochemistry, 2nd ed. Elsevier, Oxford, pp. 401–436.

Hales, T.C., Roering, J.J., 2005. Climate-controlled variation in scree production, Southern Alps, New Zealand. Geology 33, 701–704.

Hayes, J.L., Riebe, C.S., Holbrook, W.S., Flinchum, B.A., Hartsough, P.C., 2019. Porosity production in weathered rock: where volumetric strain dominates over chemical mass loss. Sci. Adv. 5. https://doi.org/10.1126/sciadv.aao0834.

Heimsath, A.M., Dietrich, W.E., Nishiizumi, K., Finkel, R.C., 1997. The soil production function and landscape equilibrium. Nature 388, 358–361.

Heimsath, A.M., DiBiase, R.A., Whipple, K.X., 2012. Soil production limits and the transition to bedrock-dominated landscapes. Nat. Geosci. 5, 210–214.

Herman, F., Rhodes, E.J., Braun, J., Heiniger, L., 2010. Uniform erosion rates and relief amplitude during glacial cycles in the Southern Alps of New Zealand, as revealed from OSL-thermochronology. Earth Planet. Sci. Lett. 297, 183–189.

Hilton, R.G., Meunier, P., Hovius, N., Bellingham, P.J., Galy, A., 2011. Landslide impact on organic carbon cycling in a temperate montane forest. Earth Surf. Process. Landf. 36, 1670–1679.

Hovius, N., Stark, C.P., Allen, P.A., 1997. Sediment flux from a mountain belt derived by landslide mapping. Geology 25, 231–234.

Hurst, M.D., Mudd, S.M., Walcott, R., Attal, M., Yoo, K., 2012. Using hilltop curvature to derive the spatial distribution of erosion rates. J. Geophys. Res., Earth Surf. 117 (F2). https://doi.org/10.1029/2011JF002057.

Hurst, M.D., Mudd, S.M., Attal, M., Hilley, G., 2013. Hillslopes record the growth and decay of landscapes. Science 341, 868–871.

Jacobson, A.D., Blum, J.D., 2003. Relationship between mechanical erosion and atmospheric CO_2 consumption in the New Zealand Southern Alps. Geology 31, 865–868.

Jacobson, A.D., Blum, J.D., Chamberlain, C.P., Craw, D., Koons, P.O., 2003. Climate and tectonic controls on chemical weathering in the New Zealand Southern Alps. Geochim. Cosmochim. Acta 67, 29–46.

Jochum, K.P., Weis, U., Schwager, B., Stoll, B., Wilson, S.A., Haug, G.H., Andreae, M.O., Enzweiler, J., 2015. Geostand. Geoanal. Res. 40, 333–350.

Kohl, C.P., Nishiizumi, K., 1992. Chemical isolation of quartz for measurement of in-situ-produced cosmogenic nuclides. Geochim. Cosmochim. Acta 56, 3583–3587.

Korup, O., 2005. Large landslides and their effect on sediment flux in South Westland, New Zealand. Earth Surf. Process. Landf. 30, 305–323.

Lal, D., 1991. Cosmic ray labeling of erosion surfaces: in situ nuclide production rates and erosion models. Earth Planet. Sci. Lett. 104, 424–439.

Larsen, I.J., Montgomery, D.R., 2012. Landslide erosion coupled to tectonics and river incision. Nat. Geosci. 57, 468–473.

Larsen, I.J., Almond, P.C., Eger, A., Stone, J.O., Montgomery, D.R., Malcolm, B., 2014. Rapid soil production and weathering in the Southern Alps, New Zealand. Science 343, 637–640.

Maher, K., Chamberlain, C.P., 2014. Hydrologic regulation of chemical weathering and the geologic carbon cycle. Science 343, 1502–1504.

McGlone, M.S., Basher, L., 2012. Holocene vegetation change at treeline, Cropp Valley, Southern Alps, New Zealand. Terra Australis 34, 343–358.

Millot, R., Gaillardet, J., Dupré, B., Allègre, C.J., 2002. The Global Control of Silicate Weathering Rates and the Coupling with Physical Erosion: New Insights from Rivers of the Canadian Shield. Earth and Planetary Science Letters, vol. 196.

Ministry for the Environment and Statistics New Zealand, 2017. Average annual rainfall, 1972–2016, Environmental Reporting, Ministry for the Environment and Statistics New Zealand. https://data.mfe.govt.nz/layer/89421-average-annual-rainfall-19722016/.

Molnar, P., Anderson, R.S., Anderson, S.P., 2007. Tectonics, fracturing of rock, and erosion. J. Geophys. Res., Earth Surf. 112. https://doi.org/10.1029/2005JF000433.

Moon, S., Perron, J.T., Martel, S.J., Holbrook, W.S., St. Clair, J., 2017. A model of three-dimensional topographic stresses with implications for bedrock fractures, surface processes, and landscape evolution. J. Geophys. Res., Earth Surf. 122 (4). https://doi.org/10.1002/2016JF004155.

Mudd, S.M., Yoo, K., 2010. Reservoir theory for studying the geochemical evolution of soils. J. Geophys. Res., Earth Surf. 115, F03030. https://doi.org/10.1029/2009JF001591.

Mudd, S.M., Attal, M., Milodowski, D.T., Grieve, S.W.D., Valters, D.A., 2014. A statistical framework to quantify spatial variation in channel gradients using the integral method of channel profile analysis. J. Geophys. Res., Earth Surf. 119 (2). https://doi.org/10.1002/2013JF002981.

Mudd, S.M., Harel, M., Hurst, M.D., Grieve, S.W., Marrero, S.M., 2016. The CAIRN method: automated, reproducible calculation of catchment-averaged denudation rates from cosmogenic nuclide concentrations. Earth Surf. Dyn. 4, 655–674.

Neely, A.B., DiBiase, R.A., Corbett, L.B., Bierman, P.R., Caffee, M.W., 2019. Bedrock fracture density controls on hillslope erodibility in steep, rocky landscapes with patchy soil cover, southern California, USA. Earth Planet. Sci. Lett. 522, 186–197.

Nibourel, L., Herman, F., Cox, S.C., Beyssac, O., Lavé, J., 2015. Provenance analysis using Raman spectroscopy of carbonaceous material: a case study in the Southern Alps of New Zealand. J. Geophys. Res., Earth Surf. 120, 2056–2079.

Norrish, K., Chappell, B.W., 1967. X-ray fluorescent spectrography. In: Zussman, J. (Ed.), Physical Methods in Determinative Mineralogy. Academic Press, San Diego, CA, pp. 161–214.

Norton, K.P., von Blanckenburg, F., 2010. Silicate weathering of soil-mantled slopes in an active Alpine landscape. Geochim. Cosmochim. Acta 74, 5243–5258.

Oeser, R.A., von Blanckenburg, F., 2020. Do degree and rate of silicate weathering depend on plant productivity? Biogeosciences 17, 4883–4917.

Perron, J.T., Royden, L., 2013. An integral approach to bedrock river profile analysis. Earth Surf. Process. Landf. 38, 570–576.

Prasicek, G., Otto, J.C., Montgomery, D.R., Schrott, L., 2014. Multi-scale curvature for automated identification of glaciated mountain landscapes. Geomorphology 209, 53–65.

Prasicek, G., Larsen, I.J., Montgomery, D.R., 2015. Tectonic control on the persistence of glacially sculpted topography. Nat. Commun. 6, 1–6.

Price-Whelan, A.M., Sipőcz, B.M., Günther, H.M., Lim, P.L., Crawford, S.M., Conseil, S., Astropy Coordination Committee, 2018. The Astropy project: building an open-science project and status of the v2.0 core package. Astron. J. 156, 123. https://doi.org/10.3847/1538-3881/aabc4f.

Raymo, M.E., Ruddiman, W.F., 1992. Tectonic forcing of late Cenozoic climate. Nature 359, 117–122.
Reynolds, R.C., 1967. Estimation of mass absorption coefficients by Compton scattering: improvement and extension of the method. Am. Mineral. 52, 1493–1502.
Riebe, C.S., Kirchner, J.W., Finkel, R.C., 2004a. Erosional and climatic effects on long-term chemical weathering rates in granitic landscapes spanning diverse climate regimes. Earth Planet. Sci. Lett. 224, 547–562.
Riebe, C.S., Kirchner, J.W., Finkel, R.C., 2004b. Sharp decrease in long-term chemical weathering rates along an altitudinal transect. Earth Planet. Sci. Lett. 218, 421–434.
Scarrow, J.W., Balks, M.R., Almond, P.C., 2014. Three soil chronosequences in recessional glacial deposits near the polar plateau, in the Central Transantarctic Mountains, Antarctica. Antarct. Sci. 26, 573–583.
Schaller, M., Ehlers, T.A., 2022. Comparison of soil production, chemical weathering, and physical erosion rates along a climate and ecological gradient (Chile) to global observations. Earth Surf. Dyn. 10, 131–151.
Stone, J.O., 2000. Air pressure and cosmogenic isotope production. J. Geophys. Res. B, Solid Earth 10, 23753–23759.
Strubble, W.T., Roering, J.J., 2021. Hilltop curvature as a proxy for erosion rate: wavelets enable rapid computation and reveal systematic underestimation. Earth Surf. Dyn. 9, 1279–1300.
von Blanckenburg, F., Schuessler, J.A., Bouchez, J., Frings, P.J., Uhlig, D., Oelze, M., Frick, D.A., Hewawasam, T., Dixon, J., Norton, K., 2021. Rock weathering and nutrient cycling along an erodosequence. Am. J. Sci. 321, 1111–1163. https://doi.org/10.2475/08.2021.01.
Walker, D., 1973. Behavior of mass absorption coefficients near absorption edges: Reynolds' method revisited. Am. Mineral. 58, 1069–1072.
West, A.J., 2012. Thickness of the chemical weathering zone and implications for erosional and climatic drivers of weathering and for carbon-cycle feedbacks. Geology 40, 811–814.
Willett, S.D., McCoy, S.W., Perron, J.T., Goren, L., Chen, C.Y., 2014. Dynamic reorganization of river basins. Science 343, 1248765. https://doi.org/10.1126/science.1248765.
Wobus, C., Whipple, K.X., Kirby, E., Snyder, N., Johnson, J., Spyropolou, K., Crosby, B., Sheehan, D., 2006. Tectonics from topography: procedures, promise, and pitfalls. In: Willett, S.D., Hovius, N., Brandon, M.T., Fisher, D.M. (Eds.), Tectonics, Climate, and Landscape Evolution: Geological Society of America Special Paper 398. In: Penrose Conference Series, pp. 55–74.
Willis, J.P., 1991. Mass absorption coefficient determination using Compton scattered tube radiation: application, limitations and pitfalls. In: Barren, et al. (Eds.), Advances in X-ray Analysis, vol. 34. Plenum Press, New York, pp. 243–261.